Available online at www.sciencedirect.com
ScienceDirect
International Journal of Heat and Fluid Flow 29 (2008) 131–148
International Journal of HEAT AND FLUID FLOW
www.elsevier.com/locate/ijhff

Active control of sprays using a single synthetic jet actuator

Anna A. Pavlova, Kiyoshi Otani, Michael Amitay *

Mechanical Aerospace and Nuclear Engineering, Rensselaer Polytechnic Institute, 110 8th Street, Troy, NY 12180, USA

Received 21 March 2007; received in revised form 11 June 2007; accepted 14 June 2007
Available online 2 August 2007

Abstract

The effect of a single synthetic jet on an air atomized solid cone spray was investigated experimentally for several spray flow rate ratios and synthetic jet momentum coefficients. Particle image velocimetry (PIV) was used to assess the effect of the synthetic jet actuation on global spray behavior, while shadowgraphy and particle tracking velocimetry (PTV) were used at 45 locations throughout the 3D spray flow field to measure its microscopic characteristics in order to understand the influence of the synthetic jet on droplet size, distribution, and concentration. The synthetic jet was able to vector the spray up to about 18° away from the jet with increased vectoring, spray width, and RMS. Shadowgraphy measurements indicate that for low flow rate ratios, small droplets are pushed across the spray, resulting in increased concentration of small droplets on the side away from the synthetic jet. For high flow rate ratios, the number of large droplets is increased along the centerline of the spray, indicating coalescence of small droplets, as they are vectored by the synthetic jet.

Keywords: Synthetic jets; Active flow control; Sprays

1. Introduction

Sprays are widely used in a variety of applications, which include such commonplace and important areas as combustion, cooling, fire extinguishing, water and chemical dispersal in agricultural settings, drug delivery, and numerous manufacturing processes, including coating, spray drying, and many others. It is therefore not surprising that there have been numerous investigations of various aspects of sprays over the years. A large number of experimental, numerical, and theoretical studies have been carried out on the basics of spray behavior in order to gain an understanding of the complex and sometimes competing processes that occur simultaneously in a spray (summarized by Sirignano, 1999). Unfortunately, most of the experimental studies produce results that are difficult to generalize due to different operational conditions. However, there is an effort underway to gain a general understanding and ability to model analytically the physical processes within specific types of sprays (e.g., Cossali, 2001, who proposed a one-dimensional model for gas entrainment into full gas sprays).

There have been an even greater number of application-specific investigations. For example, the effect of spray characteristics on spray cooling effectiveness (e.g., Ghodbane and Holman, 1991; Estes and Mudawar, 1995; Navedo, 2000; Chen et al., 2002, 2004), and in combustion applications have also been extensively studied (e.g., Kuo, 1996; Carvalho et al., 1997; Karpetis and Gomez, 1999; Hardalupas and Horender, 2001; Das and Van-Brocklin, 2003; Park et al., 2006; Panao and Moreira, 2005; Imaoka and Sirignano, 2005).

In most spray applications, spray characteristics, such as droplet size and distribution, are highly dependent on the specific spray nozzle used (Pimentel et al., 2006), which makes it difficult to alter them without a complete overhaul of the system. However, it is those characteristics that are often of utmost importance to the specific task the spray is required to accomplish (for example in reacting sprays, combustion, and agriculture). The implementation of

* Corresponding author. Tel.: +1 518 276 3340.
E-mail address: amitam@rpi.edu (M. Amitay).

0142-727X/$ - see front matter © 2007 Elsevier Inc. All rights reserved.
doi:10.1016/j.ijheatfluidflow.2007.06.004

Nomenclature

A_j	area of the synthetic jet orifice
A_s	area of the spray nozzle orifice
C_μ	momentum coefficient, $C_\mu = \frac{A_j U_o^2}{A_s U_e^2}$
d_d	droplet diameter
d_s	spray nozzle orifice diameter
f	driving (formation) frequency of synthetic jet
L_o	synthetic jet stroke length, $L_o = \int_0^\tau u(t)dt$
N_b	number of droplets, at a given size, in the baseline spray
$N_b\|_{tot}$	total number of droplets in the baseline spray
N_f	number of droplets, at a given size, in the forced spray
Q_a	air flow rate supplied to the spray nozzle
Q_w	water flow rate produced by the spray nozzle
t	time
T	period of synthetic jet actuation cycle, $T = 1/f$
$u(t)$	periodic velocity at the center of the jet exit plane
U	streamwise velocity
U_{CL}	centerline velocity of the spray
U_e	average air exit velocity at the spray orifice, $U_e = \frac{Q_a}{A_s}$
U_{max_b}	maximum centerline velocity of the baseline spray
U_o	synthetic jet's average orifice velocity, $U_o = \frac{L_o}{T}$
U_{RMS}	RMS of the streamwise component of velocity
V	cross-stream velocity
V_{RMS}	RMS of the cross-stream component of velocity
Vt_{RMS}	RMS of the total velocity in the measurement plane, $Vt_{RMS} = \sqrt{U_{RMS}^2 + V_{RMS}^2}$
x	streamwise coordinate
y	cross-stream coordinate
z	span-wise coordinate
Δt	time step
Δx	distance traveled in the streamwise direction (used in PTV)
Δy	distance traveled in the cross-stream direction (used in PTV)
δ	spray width
τ	blowing portion of the cycle, $T/2$
θ	vectoring angle

active flow control that could enable manipulation of spray behavior and parameters, as necessary, would enhance the versatility and efficiency of sprays.

However, to date, there have been a very limited number of investigations into the effect of active flow control of sprays. As was discussed by Pothos and Longmire (2002), flow control of the particulate phase of a two phase flow can be affected either directly (by a direct impact between the control mechanism and the particles) or indirectly (by controlling the spacing and size of coherent structures in the carrier fluid). For an air-assisted spray, Bachalo et al. (1993) noted that there are interactions between the spray droplets and coherent flow structures. Wang et al. (1999) used an indirect mechanism (a piezo-electric actuator inside the nozzle) to modulate the spray and affect its characteristics, concluding that it is a viable method to alter spray cone angle, droplet size and velocity, as well as spray structure. Sujith et al. (1997) investigated the behavior of droplets in axial acoustic fields (indirect mechanism), finding that the size and mean terminal velocity of the droplets are reduced in acoustic fields. In later works, Sujith (2003, 2005) showed that imposing axial acoustic fields on air atomized ethanol sprays shortens the spray, increases the spray cone angle due to entrainment into the spray, as well as reduces the droplet velocity, which the author attributes to the presence of smaller droplets and decrease in the mean drag of droplets. Miller et al. (2000) implemented a direct mechanism by using a system of four Coanda jet actuators in the outer swirl cup of a fuel injector and found that these actuators can be used to significantly increase the spreading rate of the spray.

Active flow control has also been used in combustion applications. Dubey et al. (1997) considered the influence of an acoustic field on the combustion characteristics of a hydrogen-stabilized ethanol spray in a Rijke-tube pulsed combustor. Zhu et al. (2002) numerically explored the effect of forced oscillations in combustors with spray atomizers; Ramanaryanan et al. (2003) carried out characterization of an acoustically self-excited combustor with respect to evaporation, and Benajes et al. (2005) experimentally investigated the influence of injection rate shaping on spray characteristics in a diesel common rail system. All these studies showed that active flow control is a viable method to affect the development of the spray as well as the droplets themselves (e.g., their size).

In this paper, we investigate the effect of a single synthetic jet actuator on the global behavior of an air atomized spray, as well as its effect on specific spray characteristics (such as droplet size, distribution, and concentration) on a microscopic level. In general, the synthetic jet actuator can be used as both direct and indirect mechanisms, as was recently shown by Tamburello and Amitay (2006, in press). However, in the present paper, the synthetic jet was used as a direct mechanism only (direct impact of the synthetic jet onto the droplets stream), as is discussed below.

2. Experimental setup and procedure

2.1. Experimental setup

The experiments were conducted in an enclosure having dimensions of 485 mm × 425 mm × 435 mm with an open top and a return drain in the bottom. The spray nozzle, instrumented with a flow control module, was mounted above the enclosure in order to allow for optical measurements of the spray while minimizing ricocheting of droplets off the walls and bottom that can obscure the measurements. In the present experiments, water was used as the working liquid, and the spray was created using an air-assisted siphoning atomizing nozzle from Delavan (model 30609-2), featuring an orifice diameter of 1.7 mm (the spray setup is illustrated in Fig. 1). This spray nozzle was selected due to its ability to produce an axisymmetric full cone spray with small size droplets. Furthermore, similar nozzle was used by Sujith (2003, 2005) who used acoustic excitation to affect the spray characteristics.

A constant water level reservoir was used to accommodate the spray nozzle. It is comprised of a small open top container, positioned within a larger open top container with a return drain. The smaller container was provided with a continuous supply of water that was allowed to overflow into the larger container, thereby creating a reservoir that was always filled to the same level (point of overflow) from which the nozzle siphoned the water. The larger container was mounted on a motorized, computer controlled traverse, allowing the water intake level (above the spray exit plane) to be at a range $L_w = 0$–49 cm. Thus, a precise control of the amount of water siphoned in, for a given air flow rate, was enabled. With the current setup, droplets with Weber numbers of 5–250 could be produced, where the characteristic length and velocity are the droplet diameter and droplet velocity, respectively.

Water was pumped from a 37.9 l container, equipped with a water level meter, by a diaphragm pump through a closed 7.6 l pressure vessel, which was used to damp out the unsteadiness associated with the pump, to the constant water level reservoir. Air flow to the nozzle was provided with a pressurized air line that passes through a dryer to remove the moisture and a filter to eliminate any particles larger than 5 μm, followed by a regulating valve and an in-line digital flow meter that provided precise monitoring of the volumetric air flow rate delivered to the spray nozzle.

Water mass flow rates were determined for three values of L_w used in the present experiments (0, 24.5, and 49 cm) at five air flow rates, Q_a, by collecting the water emitted from the spray nozzle for 30 s and weighing it on a precise electronic scale (with a resolution of ±0.01 g). The process was repeated three times for each set of settings, and the results were averaged. Volumetric flow rates for the water, Q_w, were then calculated from the mass flow rates.

In the present experiments, the spray was quantified by two parameters that are related: the water intake level

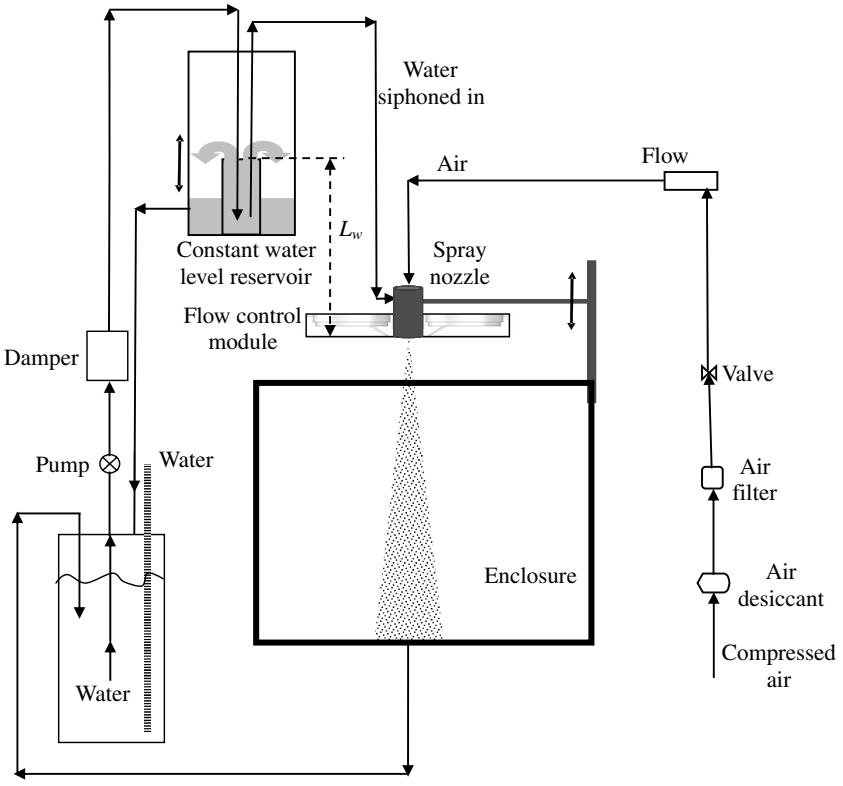

Fig. 1. Experimental setup.

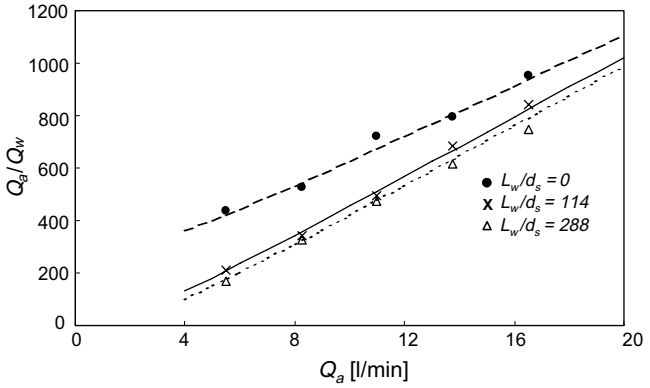

Fig. 2. The variation of the flow rate ratio with the air flow rate at three normalized water intake to nozzle orifice distances.

above the spray exit plane, L_w, and the air to water flow rate ratio, Q_a/Q_w. Fig. 2 illustrates the relationship between Q_a/Q_w and Q_a for three normalized water levels. For all three cases, the flow rate ratio varies with the air flow rate. Moreover, for a given air flow rate, increasing the normalized distance between the water level and the spray nozzle results in a decrease in Q_a/Q_w due to the increase of the amount of water that is siphoned in.

A module for active flow control was designed to fit onto the spray nozzle, such that the spray nozzle is in the center and four synthetic jet actuators are located around the circumference of the spray nozzle at 90° to each other (Fig. 3). A synthetic jet is a jet that is synthesized at the edge of an orifice by a periodic motion of a diaphragm mounted on one (or more) walls of a sealed cavity. When the diaphragm moves toward the orifice, a vortex ring is formed at the edge of the orifice, and it moves away with its own self-induced velocity such that when the diaphragm moves away from the orifice, the vortex ring is far enough away and is not affected by the fluid drawn into the cavity. Therefore, a synthetic jet has a zero-net-mass-flux per cycle of actuation but allows momentum transfer to the flow, using ambient air. With proper design, the diaphragm and the cavity are driven at resonance; thus, only small electrical power input is needed with another advantage that no plumbing or mechanical complexities are needed.

In the present experiments, the effect of a single synthetic jet was investigated and thus only a single synthetic jet was activated. The synthetic jet was formed by driving a 31.2 mm diameter piezoelectric disk, with a sinusoidal waveform at a frequency of 1100 Hz. This frequency was selected such that it corresponds to the optimal driving frequency (i.e., strongest synthetic jet with the minimum input power) for the system of the piezo disk and the cavity used in the present experiments. The Strouhal number (based on the spray nozzle diameter, the average carrier air velocity at the orifice, and the driving frequency) varies from 0.016 to 0.047 for the range of air flow rates used, which is an order of magnitude lower than the unsteady modes of the flow. Therefore, the frequency here is used only to form the jet

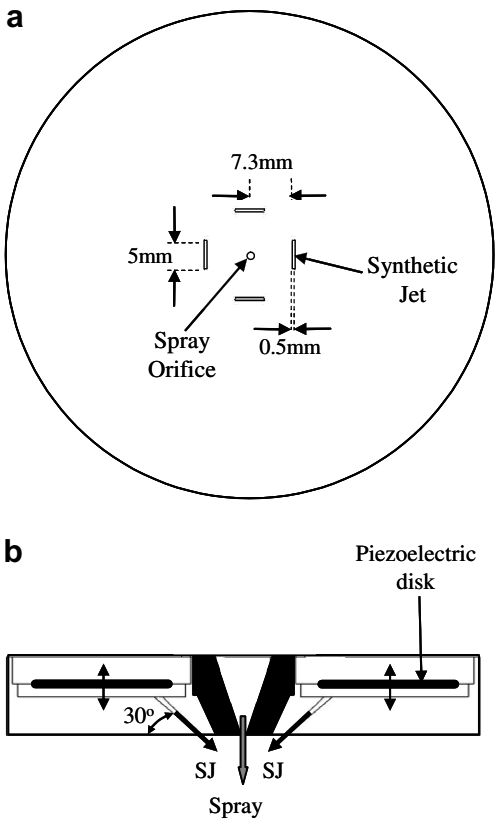

Fig. 3. Synthetic jets module: (a) top view, and (b) side view.

and not to excite the coherent structures in the carrier air flow of the spray. Hence, the flow control here is due to a direct impact of the synthetic jet onto the spray (i.e., named by Eaton and Fessler (1994) as a direct mechanism).

Each synthetic jet has a rectangular slit orifice measuring 5 mm in length and 0.5 mm in width at a distance of 7.3 mm from the spray orifice center and is inclined at an angle of 30° with respect to the nozzle plane. The angle of the synthetic jets was selected such that the synthetic jet will impact on the spray downstream of the developing region of the spray (recent work by Tamburello and Amitay (2006) on the interaction of a free jet with inclined control jets, showed a small effect of the angle of the control jets in a range of 30°–60°). The synthetic jets were calibrated using a single hot wire sensor placed in the orifice, in order to establish their momentum coefficients, defined as:

$$C_\mu = \frac{A_j U_o^2}{A_s U_e^2} \tag{1}$$

where A_j is the area of the synthetic jet orifice, A_s is the area of the spray orifice, U_e is the average air exit velocity at the spray orifice (based on the measured air flow rate), and U_o is the synthetic jet average orifice velocity, defined as:

$$U_o = \frac{L_o}{T} \tag{2}$$

where L_o is the synthetic jet stroke length, defined as

$$L_o = \int_0^{\tau} u(t)\mathrm{d}t, \tag{3}$$

where $\tau = T/2$, $T = 1/f$ is the cycle period, f is the jet's driving (formation) frequency, and $u(t)$ is the periodic velocity at the center of the jet exit plane.

2.2. Procedure: global spray measurements

Global spray measurements were carried out with PIV, which provided the velocity fields of the spray droplets for an interrogation window of 65.5 mm by 49.5 mm (with a spatial resolution of 0.38 mm). PIV data were acquired for five air flow rates, three water intake levels, and three momentum coefficients at each setting. The PIV system is based on the commercially available LaVision hardware and software and utilizes two 120 mJ Nd:YAG lasers and a 1376×1040 pixel resolution thermo-electrically cooled 12-bit CCD camera. For this portion of the experiments, the CCD camera and the laser head were placed at 90° with respect to one another. Data were acquired in two planes: perpendicular to the synthetic jet orifice (x–y plane, Fig. 4a) and parallel to the orifice (x–z plane, Fig. 4b). The laser sheet was aligned with the center of the spray, and the CCD camera was mounted perpendicular to the laser light sheet. For each case, a set of 2000 double images was recorded and averaged velocity fields were computed. In these measurements, no flow tracers were added to the air flow; therefore, the velocities that were measured in this two-phase flow were the velocities of the water droplets themselves, but not of the air present in the spray, as the water droplets are too large and heavy to faithfully follow the air motion (the average Stokes number of the droplets along the centerline is ~20). All velocity vectors were calculated using a cross-correlation technique with adaptive multi-pass, deformable interrogation windows (single pass at 32×32 and two passes at 16×16 pixels) with 50% overlap. The camera was mounted at a perpendicular distance of ~0.35 m to the laser light sheet such that the distance between pixels was 47.6 μm (for the maximum velocity of 23 m/s) in these experiments, which corresponds to an average displacement of approximately 5.5 pixels with an error of approximately ±0.1 pixel, corresponding to velocity error of ±0.4 m/s.

2.3. Procedure: detailed spray characteristics

The detailed spray characteristics (droplet size, concentration, distribution, as well as velocity of individual droplets) on a microscopic level were obtained using a method that combined shadowgraphy and particle tracking velocimetry (PTV). Shadowgraphy is a technique that is based on high resolution imaging and backlight illumination, where solids, opaque or transparent droplets, and bubbles having a diameter from 2 μm to 2000 μm can be measured. When the backlighting is created by a double-pulsed laser light, which is the case in the present work, the velocity of individual droplets can also be measured (using PTV). The laser beam passed through a diffuser, such that the droplets were illuminated from one side, and a high resolution CCD camera instrumented with a long-range microscope acquired double images of the shadows from the opposite side (Fig. 5).

The system used is the same dual-pulse laser and optical arm used for PIV, along with a special diffuser attachment for scattering the laser light. The CDD camera, with the microscope attached, and the light source are mounted on an optical table, and precise positioning of the camera is ensured by using a two-axis computer-controlled traversing mechanism. In the present experiments, the distance of the microscope from the centerline of the spray was 285 mm, resulting in an interrogation window of 1.3 mm × 1.8 mm.

The information on size, shape, and velocity from the double-image shadowgraphs was obtained using a commercial algorithm (provided by the LaVision software). In order to identify and measure only the droplets that are in the focal plane of the microscope, an intensity-based

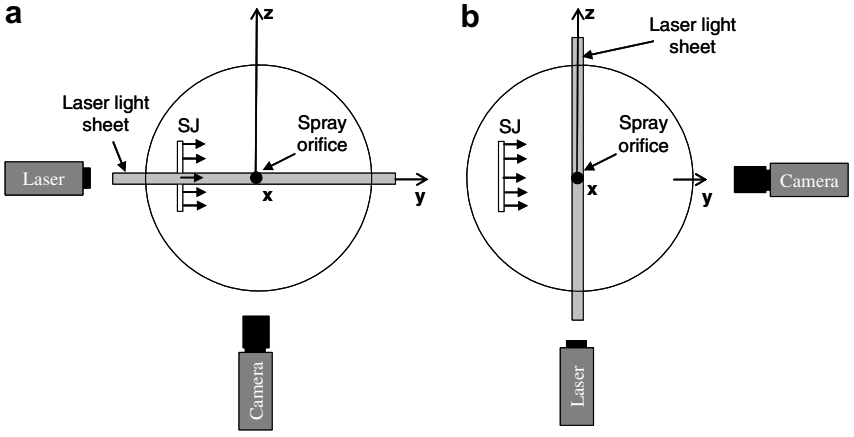

Fig. 4. Laser-camera orientation for PIV measurements in a plane: (a) perpendicular to the synthetic jet orifice (x–y plane), and (b) parallel to the jet (x–z plane).

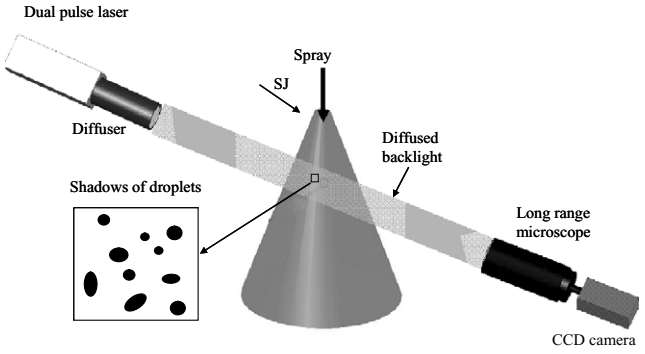

Fig. 5. Experimental setup for the Shadowgraphy technique.

filtering technique was used, as there is a fine balance between finding all particles in the focal plane and still discarding all the out-of-focus ones. In addition, restrictions on the droplet centricity, which is the ratio of the length of the minor axis to the major length of major axis of the ellipse and reflects how close the shadow of the droplet comes to a circle (larger than 60%) and droplet size (smaller than 110 μm in diameter) were used, ensuring that ligaments and clusters of droplets that appear as a single shape are not counted as individual droplets. The error associated with the sizing of droplets depends on the error in pixels associated with the system and the error that may be introduced by how the edge of the shadow is defined in processing the data, which was estimated to be at worst 0.5 pixels, where 1 pixel in the image corresponds to 1 μm, corresponding to an error in droplet diameter of 0.5 μm.

For the calculation of individual droplet velocity, three passes with the initial window size of 100 μm by 100 μm, and decreasing the window size by a factor of two with each pass, were used. In addition, a restriction on the droplet diameter difference (between two images in a pair of images) of less 7% was implemented to ensure that the droplet is identified as the same on the two images. For the PTV analysis, initial shifts of droplet motion in the horizontal and vertical directions within a shadowgraph were supplied to the algorithm, which were different for each case and each location.

Fig. 6 presents an example of a pair of raw images (Fig. 6a and b) where the second image was acquired 6.8 μs after the first image, and the processed image (Fig. 6c). Between the two images the droplets moved a certain distance in the x-direction, Δx, and a distance Δy in the y-direction (a representative droplet is marked by an arrow in Fig. 6a and as a dotted circle in Fig. 6b), and thus the total velocity of individual droplet was calculated. Fig. 6c shows the velocity and size of individual droplets (in m/s and μm, respectively) that are in focus and have the pre-defined intensity levels and restriction criteria, as discussed above. Only the droplets that appear in both images and are recognized as the same droplet have velocity vectors calculated. The average displacement was approximately 40 pixels (corresponding to 50 μm), with

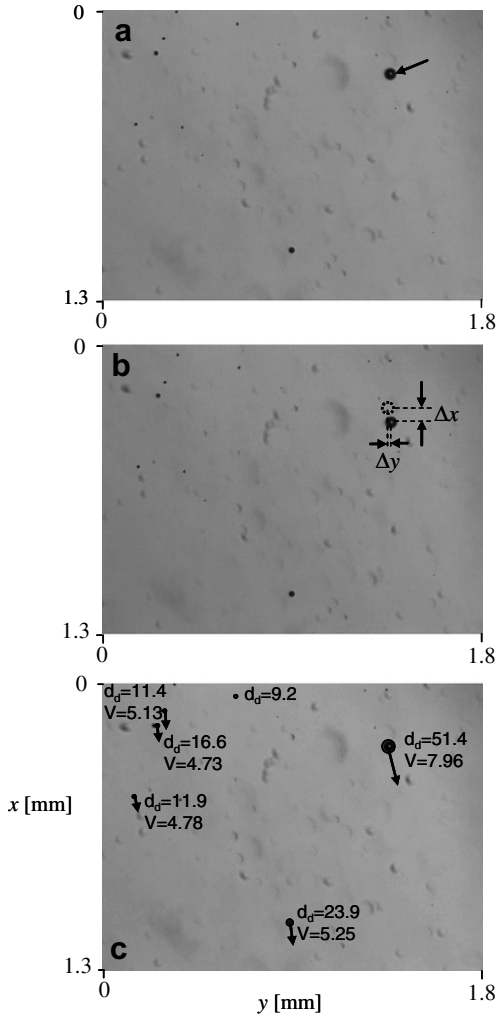

Fig. 6. Raw Shadowgraphy images at time t (a) and time $t + \Delta t$ (b), and (c) a processed image.

the maximum velocity of 27 m/s, which corresponds to the velocity error ±0.1 m/s.

Additional processing of the Shadowgraphy data was carried out using a custom-made FORTRAN code. The code sorts the droplets according to their respective size, and discards droplets that are associated with spurious velocity vectors (those that have velocity larger than their 8 neighbors by more than 50%, as well as droplets that only appear in one image of the pair). It also calculates the droplet density number distribution (or void fraction) for all droplets, as well as for a predefined droplet size range.

In the data reported here, Shadowgraphy measurements (of the baseline spray and when the synthetic jet was activated) were acquired at 45 locations in the spray, as illustrated in Fig. 7, such that the effect of active flow control could be determined for the entire three dimensional spray. Only the highest and lowest air flow rates, at a water intake level to spray nozzle level of 49 cm, were used in these experiments. For the high air flow rate, 1000 shadowgraph pairs at each location were sufficient, whereas at the low air flow rate, 2000 shadowgraph pairs were needed. The larger

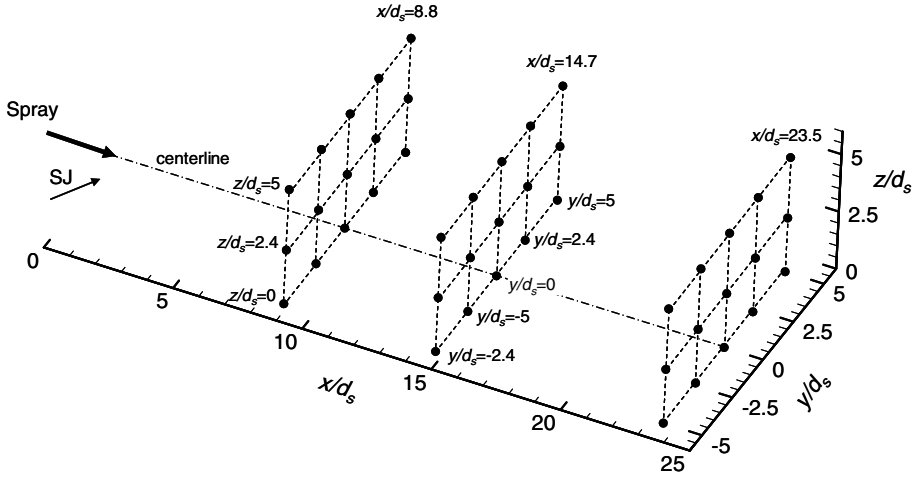

Fig. 7. Measurement locations where Shadowgraphy data were acquired.

number of images required for the low air flow rate case is a result of the spray being comprised of fewer droplets at these conditions, as compared to the spray at the high air flow rate.

3. Results

3.1. Baseline spray

First, the characteristics of the baseline spray (i.e., without flow control) were established for the nozzle used in the present work. The effect of the air to water flow rate ratio, Q_a/Q_w, on the spray velocity field was examined and is presented in Fig. 8a–c at $Q_a/Q_w = 166$, 475, and 746, respectively, where the spray is from top to bottom. For all flow rate ratios, the velocity vector field exhibits a single peak distribution, as expected, where increasing Q_a/Q_w yields higher velocities throughout the flow field, while the jet spreading decreases. Note that due to the laser light reflection from the spray nozzle, the PIV data near the orifice (i.e., $x/d_s < 2$) is unreliable and thus not presented in the plots.

To further appreciate the effect of the flow rate ratio, the downstream evolution of the centerline velocity and the width of the spray were calculated and are presented in Fig. 9a and b, respectively. Here, the centerline velocity is normalized by the maximum centerline velocity, while the width of the spray is normalized by its orifice diameter. The width of the spray is defined as the cross-stream distance between the locations to either side of the spray centerline, where the streamwise velocity is half of the maximum velocity.

For all flow rate ratios tested, the downstream development of the normalized centerline velocity consists of two distinct regions (Fig. 9a). Near the orifice, for $x/d_s < 6.5$, the centerline velocity increases very rapidly due to the momentum of the droplets, while farther downstream, the centerline velocity decays with downstream distance as $(x/d_s)^{-0.5}$, where the decay is weaker as Q_a/Q_w increases. This is consistent with the findings of Faeth et al. (1995), Karpetis and Gomez (1999), and Cossali (2001).

The downstream development of the spray width (Fig. 9b) also exhibits two distinct regions: near the orifice, where the spreading of the spray is low, and farther downstream, where the width of the spray increases linearly with downstream distance (similar to the result by Cossali, 2001). Near the orifice, the lowest Q_a/Q_w spray has the highest spreading rate, while farther downstream the spreading rate is the same for all flow rate ratios (the width of the spray increases linearly with downstream distance), even though the width of the spray (or spray angle) is smaller with increasing flow rate ratio.

3.2. Active control of the spray using a single synthetic jet actuator

Next, the effect of a single synthetic jet actuator on the spray flow field was examined. As was mentioned above, the Strouhal number, associated with the driving frequency of the synthetic jet, is an order of magnitude lower than the unsteady modes of the flow. Therefore, the mechanism by which the synthetic jet affects the spray is due to a direct impact of the synthetic jet onto the spray (i.e., direct mechanism).

Fig. 10a–c and d–f present the cross-stream distributions of the streamwise and cross-stream velocity components, respectively, at $x/d_s = 8.8, 14.7$ and 23.5 in x–y plane (see orientation in Fig. 4), for $Q_a/Q_w = 166$ and $C_\mu = 0.04$, 0.20, and 0.425. The plots of the baseline streamwise velocity exhibits a single-peak distribution, where the peak velocity decreases and the spray width increases with increasing downstream distance. The cross-stream velocity component exhibits a double peak cross-stream distribution, one peak on each side of the centerline, with opposite magnitudes, indicating the spreading of the spray. In this case the spray angle is ~27°, where the edge of the spray

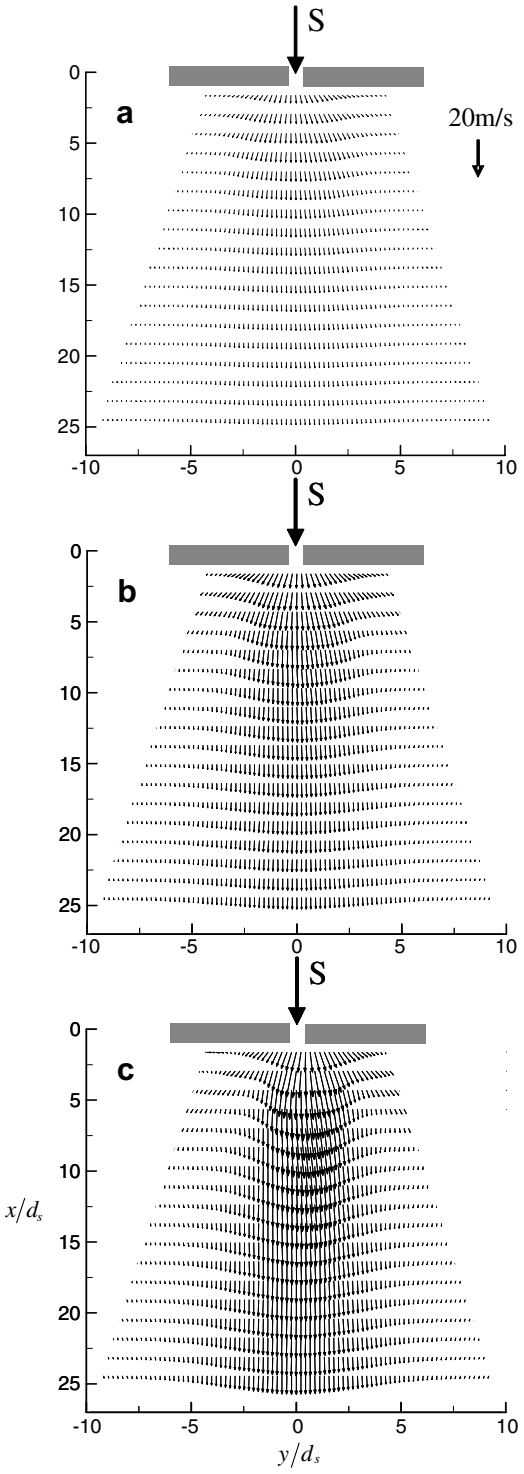

Fig. 8. Velocity vector fields of the baseline spray. $Q_a/Q_w =$ (a) 166, (b) 475 and (c) 746.

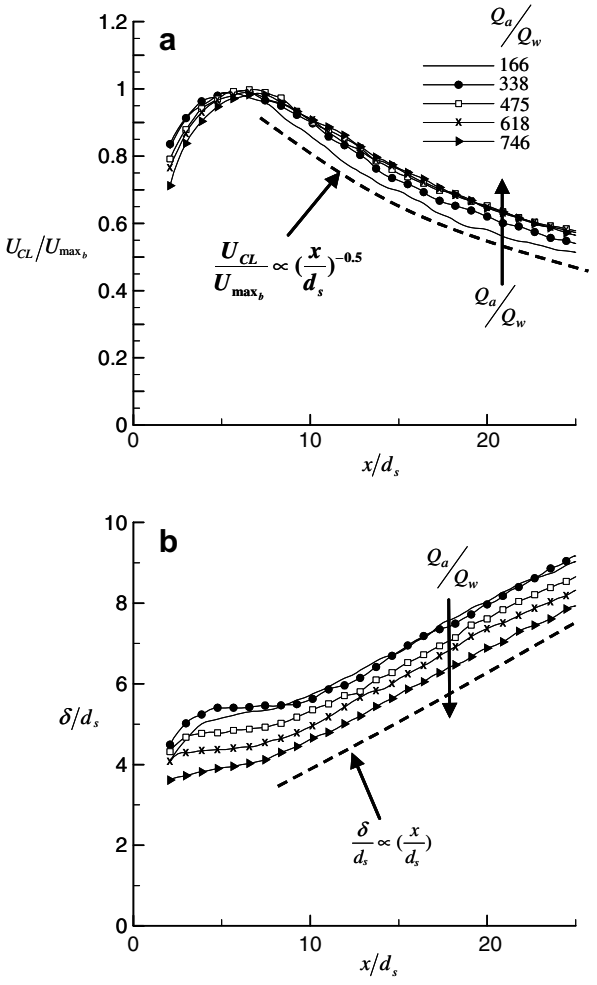

Fig. 9. Downstream development of the normalized (a) centerline velocity, and (b) spray width for various flow rate ratios. Baseline case.

is defined as the location where the streamwise velocity is 20% of the maximum velocity of the spray. This is consistent with the value of 30°, provided by the manufacturer.

When the synthetic jet is activated, the spray is vectored away from the synthetic jet, and the vectoring angle becomes larger with the increase of momentum coefficient (Fig. 10a–c). The vectoring angle is defined as the angle between the x-direction and the line that follows the location of the maximum spray velocity. Furthermore, the cross-stream velocity component is positive throughout most of the cross-stream domain, as a result of the synthetic jet impulse on the droplets.

Next, the effect of the synthetic jet on a spray with a much higher air to water flow rate ratio ($Q_a/Q_w = 746$) was examined. As will be shown later, at this high Q_a/Q_w, the spray consists of a larger amount of smaller size droplets. Furthermore, at the higher flow rate ratio, the droplets have higher velocities throughout the flow field, and since the velocity range of the synthetic jet was the same as for the spray with the lower flow rate ratio, it resulted in an order of magnitude smaller range of C_μ (0.005, 0.0225, and 0.0475, respectively). The corresponding cross-stream distributions of the streamwise and cross-stream velocity components are presented in Fig. 11a–c and d–f at $x/d_s = 8.8, 14.7$, and 23.5, respectively. Without flow control (Fig. 11a) the spray is symmetric with a spray angle of ~20° (calculated in the same way as that of the lower flow rate ratio). When the synthetic jet is activated, its effect on the velocity vector field is small

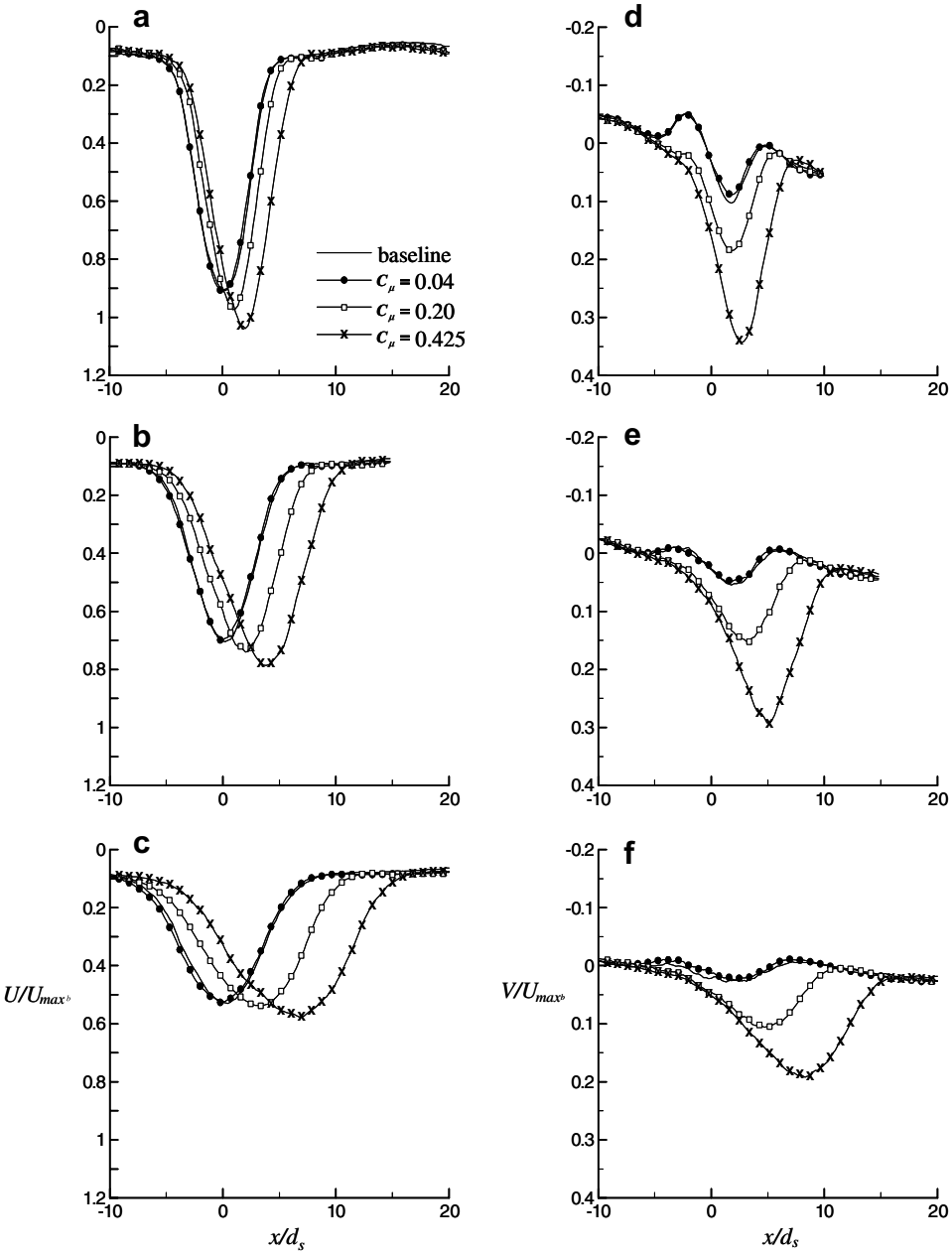

Fig. 10. Cross-stream distribution of the (a–c) streamwise and (d–f) cross-stream velocity components at $x/d_s =$ (a, d) 8.8, (b, e) 14.7, and (c, f) 23.5. $Q_a/Q_w = 166$.

compared to the low flow rate ratio spray, with the vectoring angle less than 2°. However, for a similar momentum coefficient, the effect of the synthetic jet is much larger on the spray with the high flow rate ratio (compared to the low flow rate ratio). This may be attributed to the smaller size droplets (smaller Stokes number) associated with the high Q_a/Q_w, which is more susceptive to the synthetic jet impulse.

The effect of the synthetic jet on the spray was also examined by comparing the downstream evolution of the centerline velocity, the spreading of the spray, and the trajectory of the maximum streamwise velocity with and without flow control, as presented in Fig. 12a–c ($Q_a/Q_w = 166$) and Fig. 12d–f ($Q_a/Q_w = 746$), respectively. Here, the variables are normalized in the same way as in Fig. 9, using the baseline values. When the synthetic jet is activated, for the low Q_a/Q_w, the normalized centerline velocity (Fig. 12a) is larger than that of the baseline case for $x/d_s < 6$. Further downstream, the centerline velocity decays faster than for the baseline, where the decay rate increases with larger C_μ. As Q_a/Q_w increases (Fig. 12d), the centerline velocity of the forced spray is lower than for the baseline case throughout the measurement domain. The difference in the effect of the synthetic jet for the two flow rate ratios might be due to the fact that at the low Q_a/Q_w the spray has slow moving large droplets, while at the high Q_a/Q_w

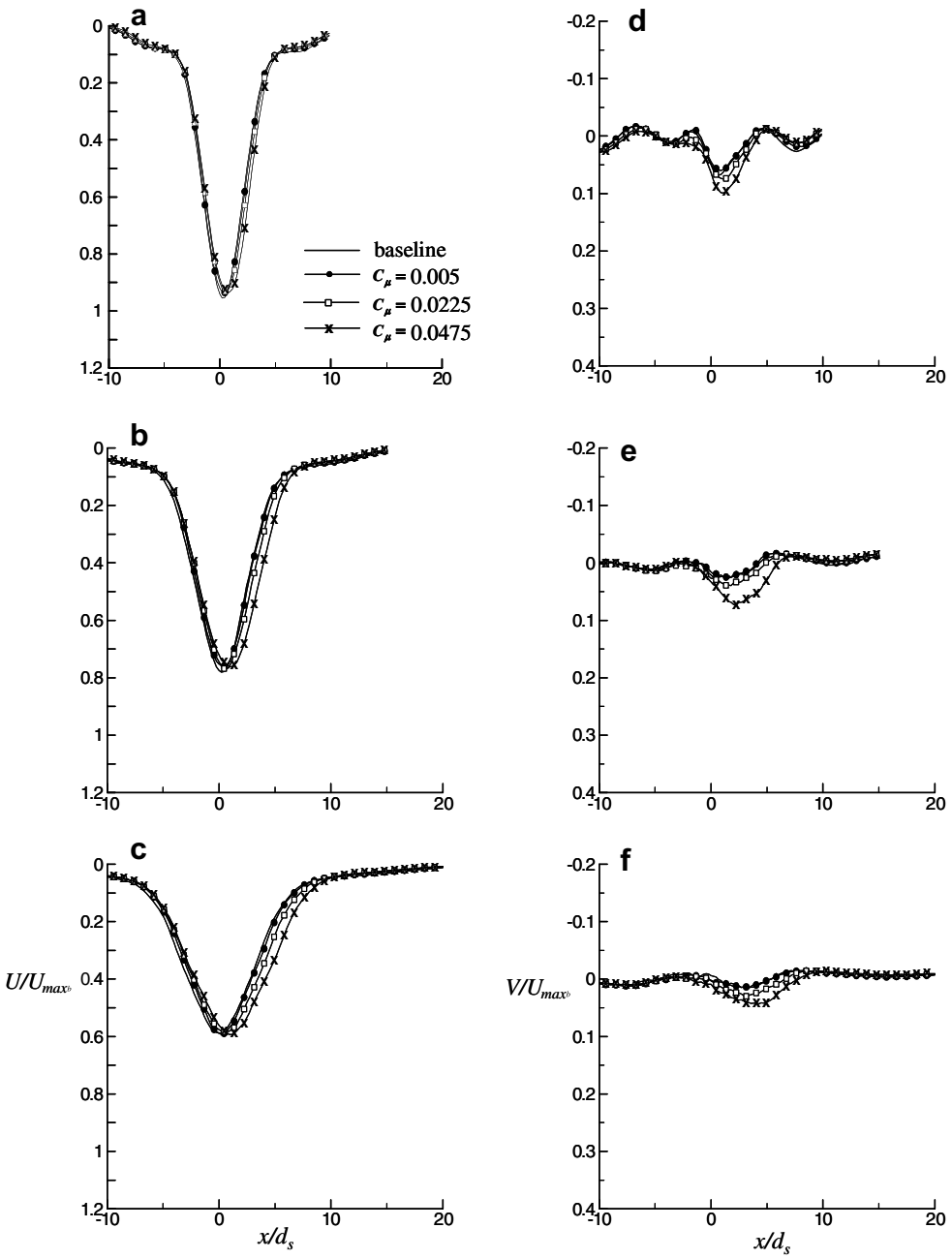

Fig. 11. Cross-stream distribution of the (a–c) streamwise and (d–f) cross-stream velocity components at $x/d_s =$ (a, d) 8.8, (b, e) 14.7, and (c, f) 23.5. $Q_a/Q_w = 746$.

the spray consists of smaller droplets, as will be discussed in conjunction with Fig. 15. Note that for $x/d_s > 15$ the decay rate of the normalized centerline velocity for all three momentum coefficient cases is similar to that of the baseline jet.

As mentioned above, the downstream growth of the spray width (Fig. 12b and e) exhibits two distinct regions (the dividing line between the two regions is marked in each plot using a dashed line). When the synthetic jet is activated, there is a small effect in the region near the orifice, while the spreading of the spray is significantly enhanced farther downstream. Note that the geometric location of the interaction between the spray and the synthetic jet is at $x/d_s = 2.5$. Furthermore, comparing the effect of the synthetic jet on the low and high flow rate ratio sprays, it is evident that for a momentum coefficient of $C_\mu = 0.0225$ (Fig. 12e) there is a much greater effect at the high Q_a/Q_w than there is at the low Q_a/Q_w, when a synthetic jet with $C_\mu = 0.04$ (almost twice as much) is used. As mentioned above, this is attributed to the difference in droplet size between the two cases, where the smaller droplets of the higher flow rate ratio are more easily affected.

The trajectories of the maximum streamwise velocity, which are a good measure of the vectoring of the spray, were calculated and are presented in Fig. 12c and f for $Q_a/Q_w = 166$ and 746, respectively. The synthetic jet has

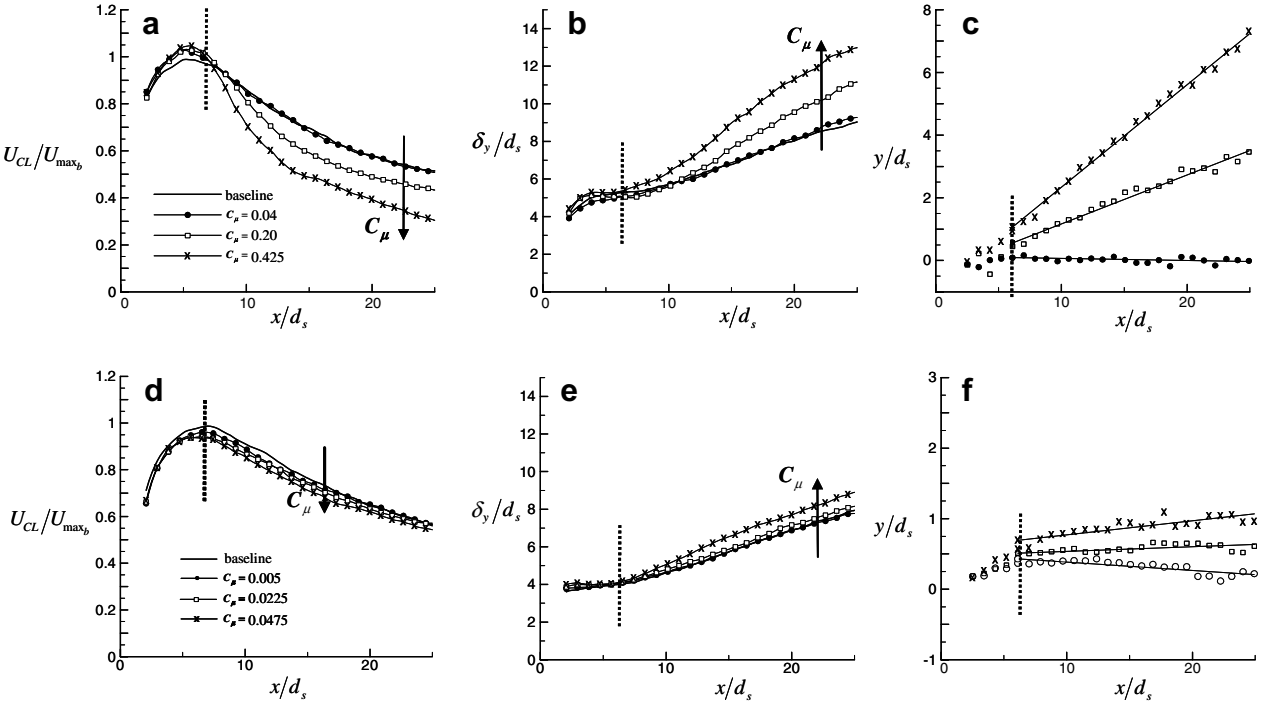

Fig. 12. Downstream development of (a, d) the centerline velocity, (b, e) the spray width, and (c, f) the trajectory of the maximum streamwise velocity. $Q_a/Q_w = $ (a–c) 166, and (d–f) 746.

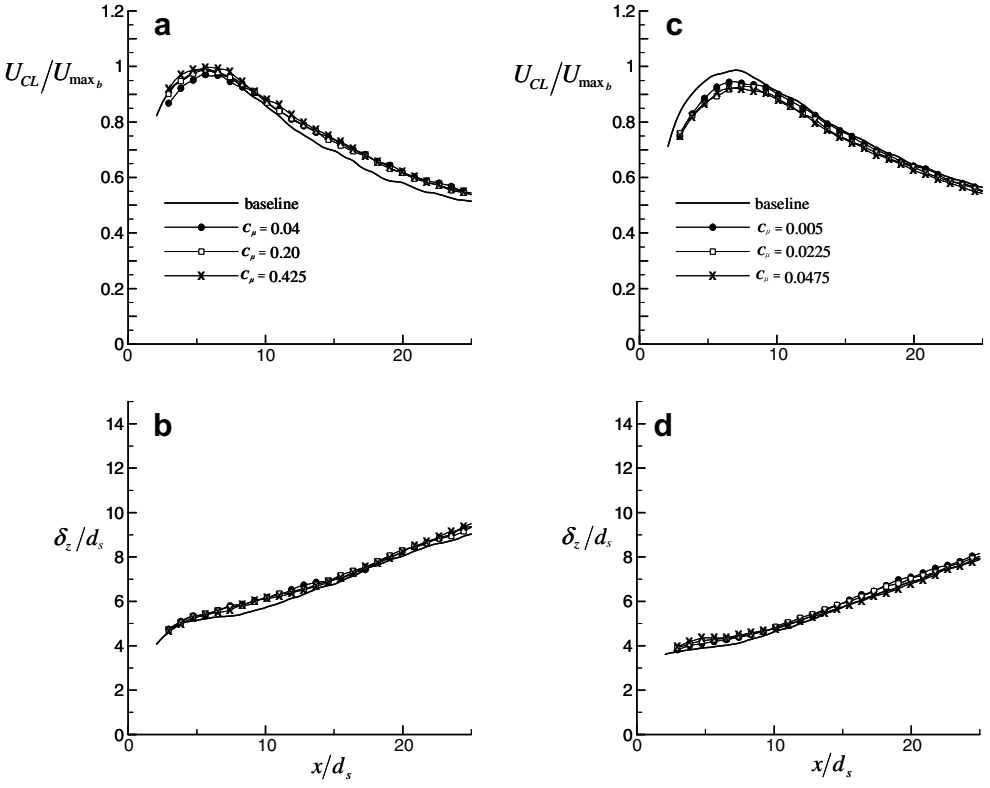

Fig. 13. Downstream development of (a, c) the centerline velocity, and (b, d) the spray width in the x–z centerline measurement plane. $Q_a/Q_w = $ (a, b) 166, and (c, d) 746.

hardly any effect in the region near the spray exit, whereas farther downstream, the location of the maximum velocity deviates from the centerline (i.e., $y/d_s = 0$) with a vectoring angle of $0.4°, 9.1°$, and $17.7°$ ($C_\mu = 0.04, 0.20$, and 0.425,

respectively) for the low flow rate ratio spray (Fig. 12c), and 0.1°, 1.1°, and 1.9° ($C_\mu = 0.005, 0.0225$, and 0.0475, respectively) for the high flow rate ratio spray.

As mentioned above, in the present paper a single synthetic jet actuator was used; therefore, the spray loses its symmetry and three-dimensionalities arise. Hence, the effect of the synthetic jet on the spray in the transverse centerline plane (x–z plane, see orientation at Fig. 4b) was examined and is presented in Fig. 13a–d for the downstream development of the centerline velocity (Fig. 13a and c) and spray width (Fig. 13b and d) at $Q_a/Q_w = 166$ (Fig. 13a and b) and 746 (Fig. 13c and d). Here, the width of the spray is denoted by δ_z to distinguish from the spray width in the x–y plane, δ_y. In this plane, the effect of the synthetic jet on the low and high Q_a/Q_w is small compared to the effect in the x–y plane. For the low Q_a/Q_w spray, the effect of the control is noticeable only in the far region ($x/d_s > 7$), where the centerline velocity increases compared to the baseline case, as the width of the spray grows slightly. For the high Q_a/Q_w spray, the effect of the flow control is mainly in the near field region ($x/d_s < 10$). In both cases, the effect is invariant of the momentum coefficient throughout most of the measurement domain.

Another important spray parameter is its RMS level. Therefore, the effect of the synthetic jet on the RMS of the total velocity in the measurement plane, Vt_{RMS}, was investigated, and is presented in Fig. 14a for the baseline case and Fig. 14b–d for the forced spray at $Q_a/Q_w = 166$ with $C_\mu = 0.04, 0.20$, and 0.425, respectively. As expected, without control, the RMS is symmetric with respect to the centerline, and it exhibits a double peak distribution (one peak on each side of centerline), essentially forming two "lobes" near the edges of the spray for $2 < x/d_s < 7$, which are attributed to the large shear at the edge of the spray. Farther downstream, the cross-stream distribution of the RMS has a single peak, where the maximum levels are around the centerline.

When the synthetic jet is activated the RMS levels increase throughout the flow field, with larger RMS levels as C_μ increases. The largest increase in the RMS levels is on the side closer to the synthetic jet. Note that the effect of the synthetic jet on the RMS levels of the high Q_a/Q_w spray is similar (for similar momentum coefficients) and is not shown here for brevity.

3.3. Control of spray parameters

Finally, the effect of the synthetic jet on the detailed spray parameters (i.e., droplet size, distribution, and concentration) was investigated at 45 locations in the spray cone (see measurement locations in Fig. 7) using the combined Shadowgraphy and PTV techniques. In these mea-

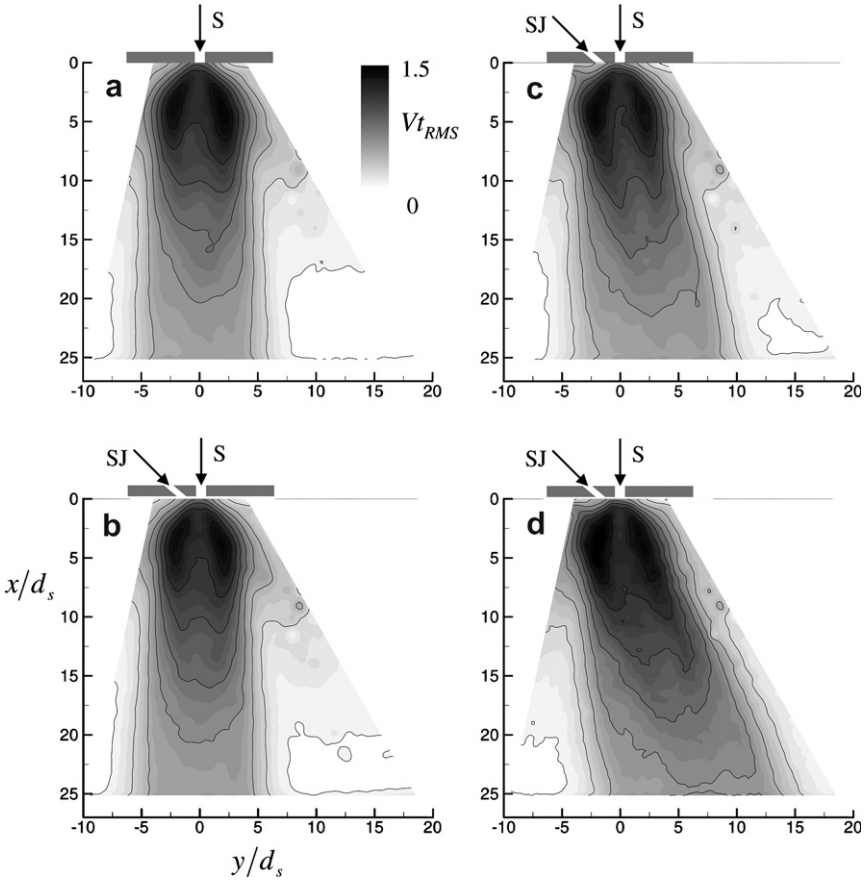

Fig. 14. Total velocity RMS fields for the (a) baseline, and the actuated cases with $C_\mu =$ (b) 0.04, (c) 0.20, and (d) 0.425. $Q_a/Q_w = 166$.

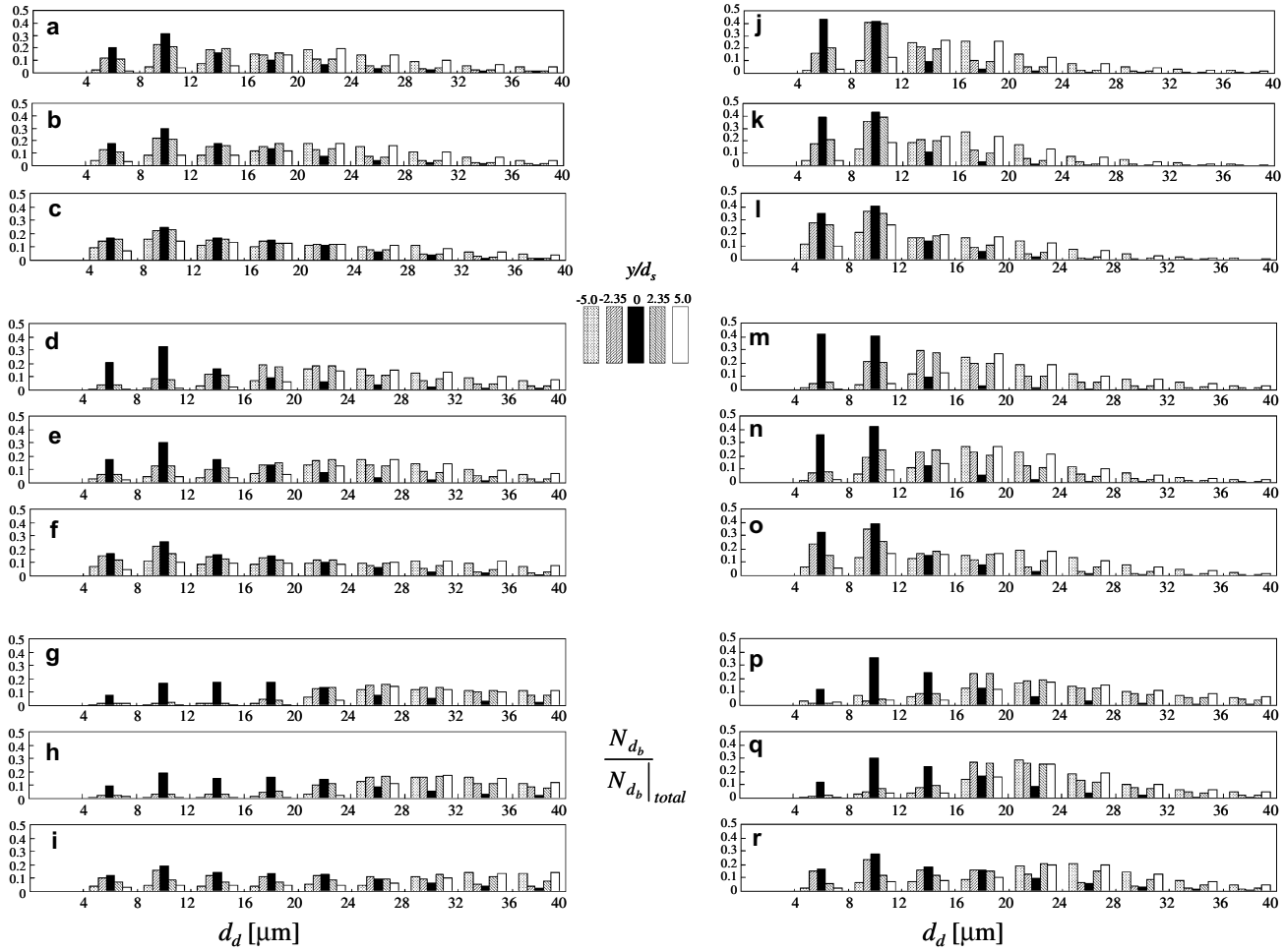

Fig. 15. Droplet size histograms for the baseline spray at $x/d_s = 8.8$ (a, d, g, j, m, p), 14.7 (b, e, h, k, n, q), and 23.5 (c, f, i, l, o, r), and at $z/d_s = 0$ (a, b, c, j, k, l), 2.35 (d, e, f, m, n, o), and 5 (g, h, i, p, q, r) for $Q_a/Q_w = 166$ (a–i) and 746 (j–r).

surements, a high magnification long range microscope was used such that high spatial resolution could be achieved (the interrogation window is 1.3 mm × 1.8 mm). The droplet size distribution histograms for the baseline spray at the low and the high flow rate ratios are presented in Fig. 15a–i and 15j–r, respectively. Here, $N_{d_b}/N_{d_b}|_{total}$ is the number of droplets at a given size range, normalized by the total number of droplets throughout the interrogation window. For each droplet size group, five cross-stream locations are presented, indicated by the different styles of bars.

For $Q_a/Q_w = 166$, in the x–y plane along the centerline ($z/d_s = 0$) and at $x/d_s = 8.8, 14.7$, and 23.5 (Fig. 15a–c), there is a high concentration of droplets having a diameter between 8 μm and 12 μm, where ~85% of the droplets have a size between 4 μm and 20 μm at all three downstream locations. For each y/d_s location, off the center to both the left and the right ($y/d_s = \pm 2.35$ and ± 5), the droplets become progressively larger with increasing distance from the spray centerline. At $y/d_s = \pm 2.35$, for all three downstream locations, the most prevalent droplet size is still between 8 μm and 12 μm; however, there are more droplets of larger diameters than at the centerline. Farther off the centerline (at $y/d_s = \pm 5$), there is a high concentration of droplets with a diameter between 20 μm and 24 μm. Note the symmetric distribution of droplets about the spray centerline.

In the x–y plane at $z/d_s = 2.35$ (off the centerline, Fig. 15d–f), the droplets at $y/d_s = 0$ retain the same trend as those at $z/d_s = 0$, but there are clearly fewer droplets of smaller diameters for both $y/d_s = \pm 2.35$ and ± 5 at $x/d_s = 8.8$ and 14.7 (Fig. 15d and e), where the largest concentration of droplets is between 24 μm and 28 μm. Farther downstream, ($x/d_s = 23.5$, Fig. 15f), the droplet size distribution at all five y/d_s locations is more uniform than at the other two downstream locations.

At the measurement location farthest from the centerline plane (in the x–y plane of $z/d_s = 5$) at $x/d_s = 8.8$ and 14.7 (Fig. 15g and h, respectively), there are less droplets of diameters between 4 μm and 24 μm at $y/d_s = 0$, whereas at the other y/d_s locations, the majority of the droplets are much larger (20 μm to 40 μm).). Farther downstream (at $x/d_s = 23.5$, Fig. 15i), the droplet distribution at all five y/d_s locations is more uniform than at the other two downstream locations.

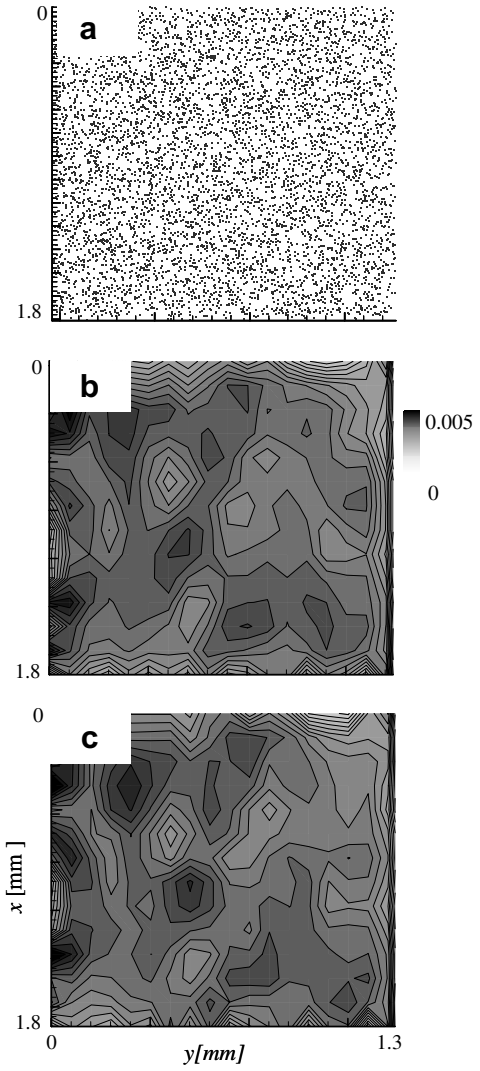

Fig. 16. Droplet distribution for $Q_a/Q_w = 166$; (a) droplet locations in the measurement window and droplet density number maps for (b) all droplet sizes, and (c) the most prevalent size group 4–20 μm.

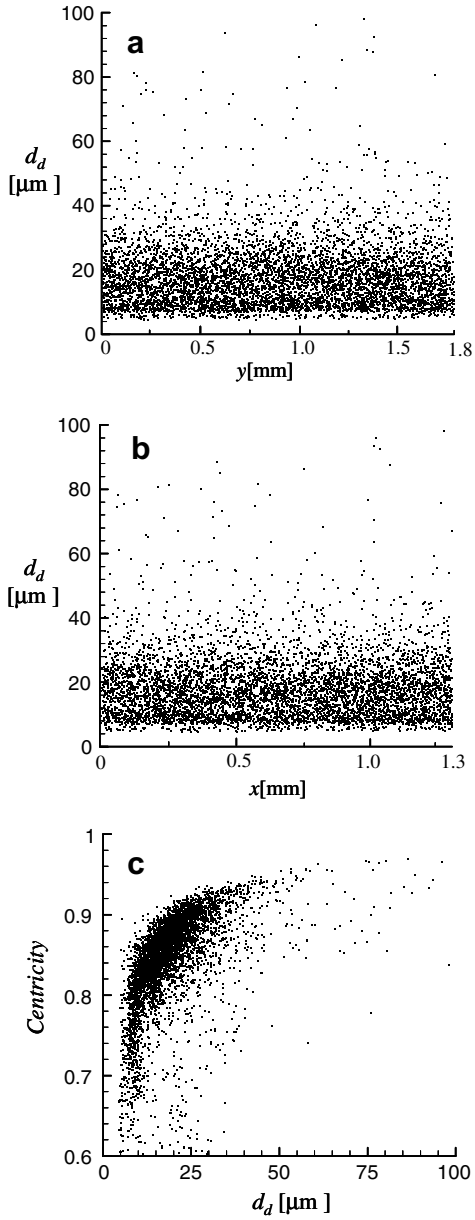

Fig. 17. Droplet diameter distributions along the (a) horizontal axis, (b) vertical axis, and (c) droplet centricity as a function of droplet size. $Q_a/Q_w = 166$.

Overall, the droplets are more uniformly distributed farther downstream, at $x/d_s = 23.5$, for all three x–y planes, with smaller droplets concentrated at the centerline while the off centerline region is populated by larger droplets. This is due to coalescence of small droplets at the lower speed regions near the edges of the spray.

For the high flow rate ratio of $Q_a/Q_w = 746$, at the centerline x–y plane ($z/d_s = 0$, Fig. 15j–l), the droplet size distributions are similar to those of the low flow rate ratio spray, except that the most frequently occurring droplet diameter range at the centerline is smaller (about 85% of the droplets have a diameter between 4 μm and 12 μm). Off centerline, the majority of the droplets have a diameter of 8–12 μm and 12–20 μm for $y/d_s = \pm 2.35$, and ±5, respectively. The smaller droplet sizes are evident at other z/d_s locations, as well, and are a result of finer atomization of the water by the nozzle at the higher air flow rate. At $z/d_s = 2.35$ (Fig. 15m–o), while the droplet size distribution along the centerline is very similar to the $z/d_s = 0$ case, at all three downstream locations, the droplets at y/d_s away from the center exhibit a shift toward larger diameters. At farthest out x–y plane ($z/d_s = 5$, Fig. 15p–r), although there are still more small droplets at the centerline, the most frequently encountered droplet diameter range for other y/d_s locations is 16–28 μm. Thus, although the droplet size trends are similar for the low flow rate spray, the droplets are, on the average, smaller than in the lower flow rate ratio spray for all measured locations.

The data for the histograms presented in Fig. 15 were averaged over the interrogation domain (1.3 × 1.8 mm), which can affect the spatial resolution of the measurements. Therefore, the spatial integrity of the histograms,

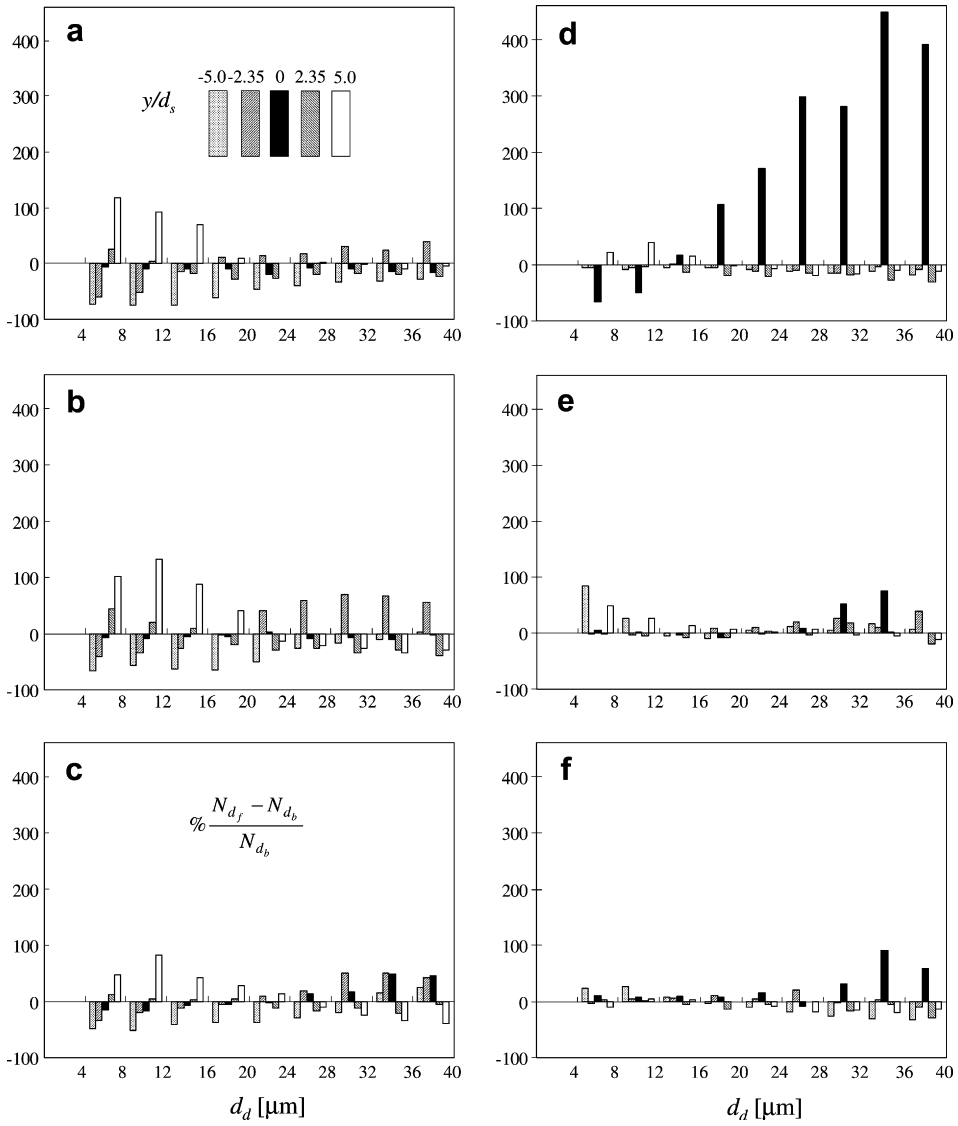

Fig. 18. Histograms of the change of the droplet size distribution (WRT the baseline) at $x/d_s = $ (a, d) 8.8, (b, e) 14.7, and (c, f) 23.5, at $z/d_s = 0$ for (a–c) $Q_a/Q_w = 166$ with $C_\mu = 0.425$, and (d–f) $Q_a/Q_w = 746$ with $C_\mu = 0.0475$.

representing the various size classes at different locations within the spray, was verified and is demonstrated for the low flow rate ratio case at $x/d_s = 23.5$ in the centerline of x–y plane in Figs. 16 and 17 (similar results were obtained at the other measurement locations and are not shown here for brevity).

Fig. 16a illustrates the locations, within the Shadowgraphy measurement window, where droplets were found, and clearly the droplets are evenly distributed throughout the measurement domain (all the measurement locations that were used in the present work were away from the edges of the spray, where droplets are sparse). Fig. 16b and c show the droplet number density maps for all droplet sizes found and for the most frequently encountered size (4–20 μm) in the baseline spray along the centerline, respectively. The droplet number density is defined as the ratio of the number of droplets of a certain size category in a grid square (here, 100 μm by 100 μm) to the total number of droplets found in the measurement domain. These maps show that all the droplets found are uniformly distributed throughout the measurement window, and that the distribution of droplet size categories is also uniform and random throughout, justifying the size of the interrogation window that was selected.

Fig. 17a and b show the distribution of the droplet diameter across the measurement window and in the streamwise direction, respectively, while Fig. 17c presents the centricity of the droplets, based on their size. Fig. 17a and b confirm that for a given droplet size, there is no spatial preference in both directions. As was also shown in the histogram (Fig. 15 above), the majority of the droplets are between 8 μm and 24 μm. Fig. 17c shows a typical relationship between droplet diameter and the centricity of the droplet, where centricity is defined as the ratio of minor

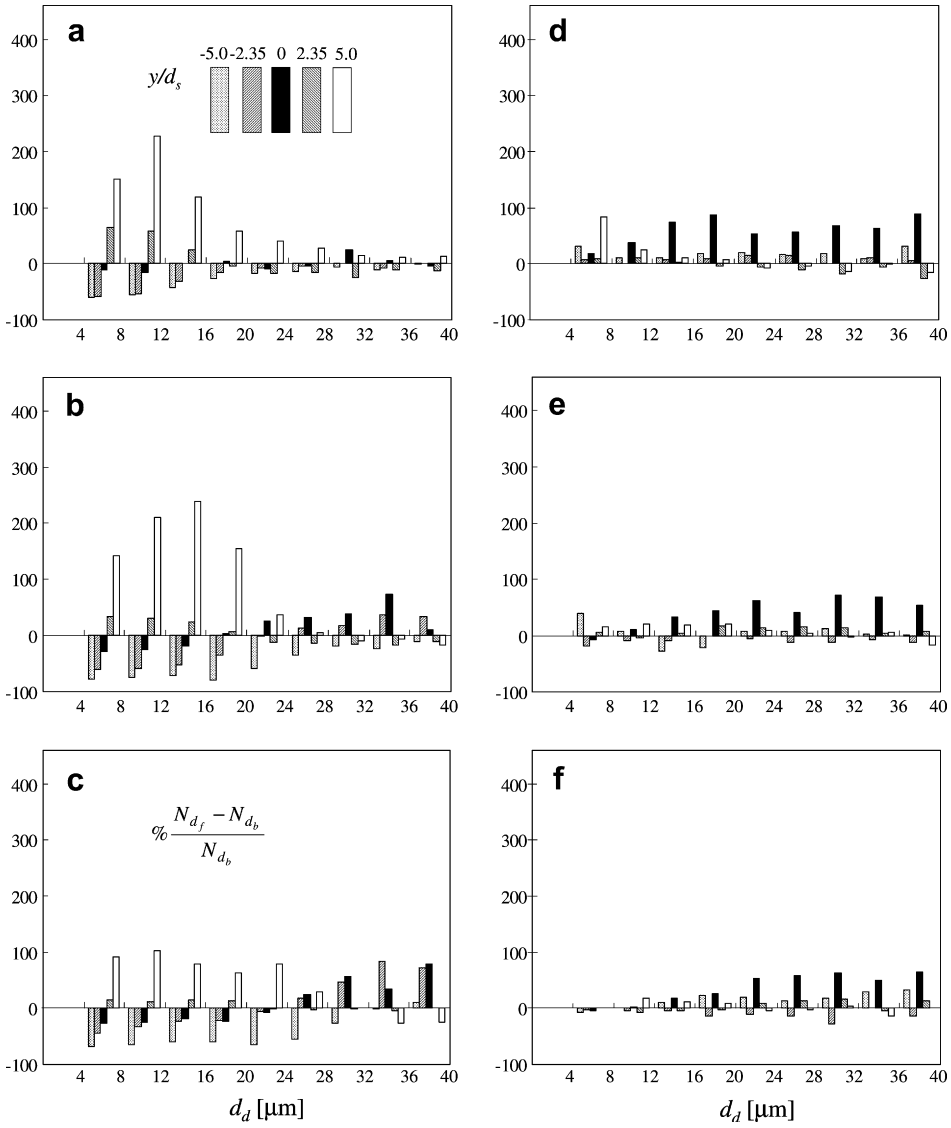

Fig. 19. Histograms of the change of the droplet size distribution (WRT the baseline) at $x/d_s = $ (a, d) 8.8, (b, e) 14.7, and (c, f) 23.5, at $z/d_s = 2.35$ for (a–c) $Q_a/Q_w = 166$ with $C_\mu = 0.425$, and (d–f) $Q_a/Q_w = 746$ with $C_\mu = 0.0475$.

to major axes within the droplet. This plot illustrates that most droplets found have a centricity between 0.75 and 0.95, and it is the smaller droplets that are less spherical, thus verifying that droplet clusters and ligaments are not counted as larger droplets. Similar results were obtained for higher Q_a/Q_w sprays and are not shown here for brevity.

Next, the effect of the synthetic jet on the droplet size and distribution at the same 45 measurement locations was examined. Here, the synthetic jet was issued from the left side of the spray (i.e., $-y/d_s$). The histograms illustrate the percentage change (with respect to the baseline case) in the droplet diameter for the controlled cases at three different z/d_s locations, $\%(N_{d_f} - N_{d_b})/N_{d_b}$, in Figs. 18 and 19 for $Q_a/Q_w = 166$ with $C_\mu = 0.425$ and $Q_a/Q_w = 746$ with $C_\mu = 0.0475$. N_{d_b} and N_{d_f} are the number of droplets (for a given group size) in the interrogation window for the baseline and forced cases, respectively. For both flow rate ratios and all the measured locations, there is clearly an effect on the droplet size distribution and on the number of droplets due to the activation of the synthetic jet.

In the x–y centerline plane ($z/d_s = 0$, Fig. 18a–c), for $Q_a/Q_w = 166$, at all three downstream locations, there is a decrease in the number of small droplets on the left side of the spray (i.e., the side closer to the synthetic jet) and an increase of those same small droplets on the right side of the spray, indicating that small droplets ($4\ \mu m \leqslant d_d \leqslant 16\ \mu m$) are pushed to the right side of the spray (i.e., away from the synthetic jet) due to the impulse of the synthetic jet on the droplets. Also, there are more droplets of large diameters to the left of the spray centerline and fewer to the right side, compared to spray without flow control. A plausible explanation for this is that as the small droplets are pushed towards the spray centerline, some of them

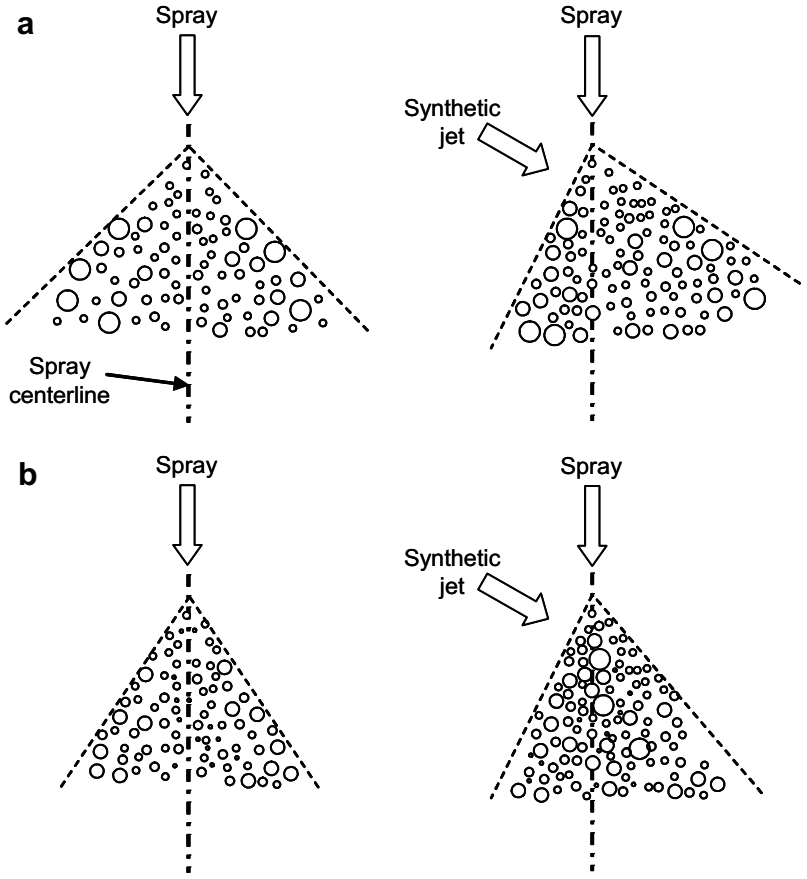

Fig. 20. Cartoons of the effect of the synthetic jet on the distribution of the droplets; (a) $Q_a/Q_w = 166$ and (b) $Q_a/Q_w = 746$. The left column shows the baseline sprays, while the right column represents the forced cases.

coalesce with other droplets on the left side of the spray, creating larger droplets.

For the high flow rate ratio spray ($Q_a/Q_w = 746$, Fig. 18d–f) there is a drastically different effect. At the centerline ($y/d_s = 0$) there is a significant increase in the number of droplets with large diameters at all three downstream locations; especially closer to the spray nozzle at $x/d_s = 8.8$ (Fig. 18d), where the increase in droplets of 32–36 μm is up to 450% compared to the baseline, accompanied by a decrease in droplets of diameters 8–12 μm. This difference from the low flow rate ratio spray is most likely due to the fact that the C_μ of the synthetic jet for $Q_a/Q_w = 746$ is much smaller, and thus it does not have enough strength to push many of the droplets past the center of the spray, causing the droplets at that location to coalesce into larger droplets.

At the x–y plane off the centerline ($z/d_s = 2.35$, Fig. 19a–c) for the low flow rate ratio, the change of the droplet size (when flow control is applied) is similar to that at $z/d_s = 0$, except that the increase of smaller droplets at $y/d_s = 5$ is even more dramatic (up to 230% at $x/d_s = 8.8$, Fig. 19a, and $x/d_s = 14.7$, Fig. 19b), whereas the increase of larger sized droplets is not as pronounced. In the case of high flow rate ratio ($Q_a/Q_w = 746$ at $z/d_s = 2.35$, Fig. 19d–f), for $x/d_s = 8.8$ there is an increase in the number of droplets of $d_d > 20$ μm up to 100% at the farthest from the synthetic jet location and an increase in the number of droplets of all diameters at $y/d_s = 0$ (Fig. 19d). At the other two downstream locations (Fig. 19e–f), there is a similar trend.

In summary, the synthetic jet has a significant effect on droplet size distribution of the spray at both flow rate ratios, but the way the synthetic jet affects the two cases is very different, due to an almost ten-fold difference in C_μ associated with the two cases, combined with the different spray droplet sizes associated with each flow rate. The mechanism by which the synthetic jet affects the droplets is due to the direct impact (i.e., transfer of momentum to the droplets and the carrier air). For $Q_a/Q_w = 166$ (see cartoon in Fig. 20a), small droplets are pushed away from the synthetic jet, across the centerline, and in the process some of them coalesce and form larger droplets on the side near the synthetic jet. For $Q_a/Q_w = 746$ (see cartoon in Fig. 20b), the droplets are smaller, they move faster, and the spreading of the spray is smaller than the lower flow rate ratio spray. Furthermore, the momentum coefficient is much smaller; thus, the impulse of the synthetic jet is not strong enough to move the small droplets all the way across the centerline of the spray, resulting in coalescence occurring around the centerline of the spray, as seen by the significant increase of the number of larger droplets at this location.

This is analogous with the spray behavior in a cross flow, described by Ghosh and Hunt (1998), as the synthetic jet in the present work introduces a cross-stream and streamwise flow component into the spray.

4. Summary and conclusions

An experimental investigation of active flow control on air atomized full cone sprays using a single synthetic jet actuator was conducted. The effect of spray flow rate ratio and the synthetic jet momentum coefficient on the global and detailed behavior of the spray was investigated using PIV and Shadowgraphy. The mechanism associated with the interaction between the spray droplets and the synthetic jet is due to a direct impact of the synthetic jet onto the spray. This interaction results in a change in the spray width, streamwise, cross-stream, and centerline droplets velocities, as well as the velocity RMS levels. Furthermore, alteration of the droplets size distribution and concentration throughout the spray was achieved.

The major conclusion of this work is that active flow control, via fluidic actuation, using a single synthetic jet actuator is feasible in controlling a free spray. The effect of flow control depends mainly on the relative strength of the jet with respect to the strength of the spray (defined in the present paper as the momentum coefficient). This technique can be used as a tool to control sprays for various applications such as spray cooling, agriculture (pesticide spraying), fuel injectors, and many more.

References

Bachalo, W.D., Bachalo, E.J., Hanscom, J.M., Sankar, S.V., 1993. An investigation of spray interactions with large-scale eddies. AIAA paper 930696.

Benajes, J., Payri, R., Molina, S., Soare, V., 2005. Investigation of the influence of injection rate shaping on the spray characteristics in a diesel common rail system equipped with a piston amplifier. J. Fluid Eng. 127, 1102–1110.

Carvalho Jr., J.A., McQuay, M.Q., Gotac, P.R., 1997. The interaction of liquid reacting droplets with the pulsating flow in a Rijke-tube combustor. Combust. Flame 108, 87–103.

Chen, R.-H., Chow, L.C., Navedo, J.E., 2002. Effects of spray characteristics on critical heat flux in subcooled water spray cooling. Int. J. Heat Mass Transfer 45, 4033–4043.

Chen, R.-H., Chow, L.C., Navedo, J.E., 2004. Optimal spray characteristics in water spray cooling. Int. J. Heat Mass Transfer 47, 5095–5099.

Cossali, G.E., 2001. An integral model for gas entrainment into full cone sprays. J. Fluid Mech. 439, 353–366.

Das, S., VanBrocklin, P.G., 2003. Effect of design and operating parameters on the spray characteristics of an outward opening injector. In: Proceedings of the 13th International Multidimensional Engine Modeling User's Group Meeting, Detroit, MI, pp. 1–6.

Dubey, R.K., Black, D.L., McQuay, M.Q., Carvalho Jr., J.A., 1997. The effect of acoustics on an ethanol spray flame in a propane-fired pulse combustor. Combust. Flame 110, 25–39.

Eaton, J.K., Fessler, J.R., 1994. Preferential concentration of particles by turbulence. Int. J. Multiphase Flow 20 (Suppl.), 169–209.

Estes, K.A., Mudawar, I., 1995. Comparison of two-phase electronic cooling using free jets and sprays. J. Electron. Packag. 117, 323–332.

Faeth, G.M., Hsiang, L.-P., Wu, P.-K., 1995. Structure and breakup properties of sprays. Int. J. Multiphase Flow 21, 99–127.

Ghodbane, M., Holman, J.P., 1991. Experimental study of spray cooling with freon-113. Int. J. Heat Mass Transfer 34, 1163–1174.

Ghosh, S., Hunt, J.C.R., 1998. Spray jets in a cross-flow. J. Fluid Mech. 365, 109–136.

Hardalupas, Y., Horender, S., 2001. Phase Doppler anemometer for measurements of deterministic spray unsteadiness. Part. Sys. Charact. 18, 205–215.

Imaoka, R.T., Sirignano, W.A., 2005. Transient vaporization and burning in dense droplet arrays. Int. J. Heat Mass Transfer 48, 4354–4366.

Karpetis, A.N., Gomez, A., 1999. Self-similarity, momentum scaling and Reynolds stress in non-premixed turbulent spray flames. J. Fluid Mech. 397, 231–258.

Kuo, K.K. (Ed.), 1996. Recent advances in spray combustion Progress in Astronautics and Aeronautics, vol. 166, p. 171.

Miller, M.F., McManus, K.R., Allen, M.G., 2000. An Aerodynamic control system for modifying fuel spray distributions. AIAA Paper 2000-0192.

Navedo, J., 2000. Parametric effects of spray characteristics on spray cooling heat transfer. Ph.D. dissertation, University of Central Florida.

Panao, M.R.O., Moreira, A.L.N., 2005. Thermo- and fluid dynamics characterization of spray cooling with pulsed sprays. Exp. Therm. Fluid Sci. 30, 79–96.

Park, S.W., Kim, S., Lee, C.S., 2006. Breakup atomization characteristics of monodispersed diesel droplets in a cross-flow stream. Int. J. Multiphase Flow 32, 807–822.

Pimentel, R.G., deChamplain, A., Kretschmer, D., Stowe, R.A., Harris, P.G., 2006. Generalized formulation for droplet size distribution in a spray. AIAA paper 2006-4918.

Pothos, S., Longmire, E.K., 2002. Control of a particle-laden jet using a piezo-electric actuator. In: Proceedings of the 11th International Symposium on Applications of Laser Techniques to Fluid Mechanics, Lisbon, July 2002.

Ramanaryanan, B., Sujith, R.I., Chakravarthy, S.R., 2003. Characterization of an acoustically self-excited combustor for spray evaporation. AIAA paper 2003-502.

Sirignano, W.A., 1999. Fluid Dynamics and Transport of Droplets and Sprays. Cambridge University Press.

Sujith, R.I., 2003. An experimental investigation of interaction of sprays with acoustic fields using PIV. AIAA paper 2003-0318.

Sujith, R.I., 2005. An experimental investigation of interaction of sprays with acoustic fields. Exp. Fluids 38, 576–587.

Sujith, R.I., Walherr, G.A., Jagoda, J.I., Zinn, B.T., 1997. An experimental investigation of the behavior of droplets in axial acoustic fields. J. Vibrat. Acoust. 119, 285–292.

Tamburello, D., Amitay, M., 2006. Manipulation of an axisymmetric jet using a synthetic jet actuator. AIAA paper 2006-3700.

Tamburello, D., Amitay, M., 2006. Manipulation of an axisymmetric jet using continuous control jets. J. Turbulence 7, 59.

Tamburello, D., Amitay, M., in press. Three dimensional interactions of a free jet with a perpendicular synthetic jet. J. Turbulence.

Wang, D., Ganji, A.R., Sipperley, C.M., Edwards, C.F., 1999. Effects of nozzle geometry and ambient pressure on the characteristics of a modulated spray. AIAA paper 99-0366.

Zhu, M., Dowling, A.P., Bray, K.N.C., 2002. Forced oscillations in combustors with spray atomizers. J. Eng. Gas Turbine Power 124, 20–30.